# FINITE ELEMENT FLOW-THERMAL-STRUCTURAL ANALYSIS OF AERODYNAMICALLY HEATED LEADING EDGES

Pramote Dechaumphai and Allan R. Wieting
NASA Langley Research Center
Hampton, Virginia

Ajay K. Pandey
Planning Research Corporation
Hampton, Virginia

# GOAL

Hypersonic vehicles operate in a hostile aerothermal environment which has a significant impact on their aerothermostructural performance. Significant coupling occurs between the aerodynamic flow field, structural heat transfer, and structural response creating a multidisciplinary interaction. A long term goal of the Aerothermal Loads Branch at the NASA Langley Research Center is to develop a computational capability for integrated fluid, thermal and structural analysis of aerodynamically heated structures. The integrated analysis capability includes the coupling between the fluid and the structure which occurs primarily through the thermal response of the structure, because (1) the surface temperature affects the external flow by changing the amount of energy absorbed by the structure, and (2) the temperature gradients in the structure result in structural deformations which alter the flow field and attendant surface pressures and heating rates.

In the integrated analysis, a finite element method is used to solve: (1) the Navier-Stokes equations for the flow solution, (2) the energy equation of the structure for the temperature response, and (3) the equilibrium equations of the structure for the structural deformation and stresses. See figure 1. Recent progress in the development of the capability is described in Ref. 1.

## DEVELOP CAPABILITY FOR INTEGRATED FLUID-THERMAL-STRUCTURAL ANALYSIS FOR AERODYNAMICALLY HEATED STRUCTURES

● INCLUDE FLOW, STRUCTURAL HEAT TRANSFER AND STRUCTURAL DEFORMATION INTERACTIONS

● USE FINITE ELEMENT METHOD:
  - NAVIER-STOKES EQUATIONS FOR FLOW
  - ENERGY EQUATION FOR HEAT TRANSFER
  - EQUILIBRIUM EQUATIONS FOR STRUCTURAL RESPONSE

Figure 1

## INTEGRATED FLUID-THERMAL-STRUCTURAL
## ANALYSIS APPROACH

The integrated fluid-thermal-structural finite element analysis approach is illustrated in figure 2 on an actively cooled scram jet engine structure. A general automated unstructured gridding technique is used to discretize the aerodynamic and coolant flow field and the structure for the thermal and structural analyses. A transient vectorized finite element algorithm is used to solve the nonlinear disciplinary equations for the solutions of the aerodynamic flow, the aerothermal loads, and the structural response. Simultaneous solution of all three disciplines is possible if required. Adaptive refinement techniques based on error indicators are applied in the analysis process to minimize the problem size and to help provide accurate and economical solutions. Several color graphic techniques are used to display the results. This integrated approach is available in a code named LIFTS, an acronym for Langley Integrated Fluid-Thermal-Structural analyzer.
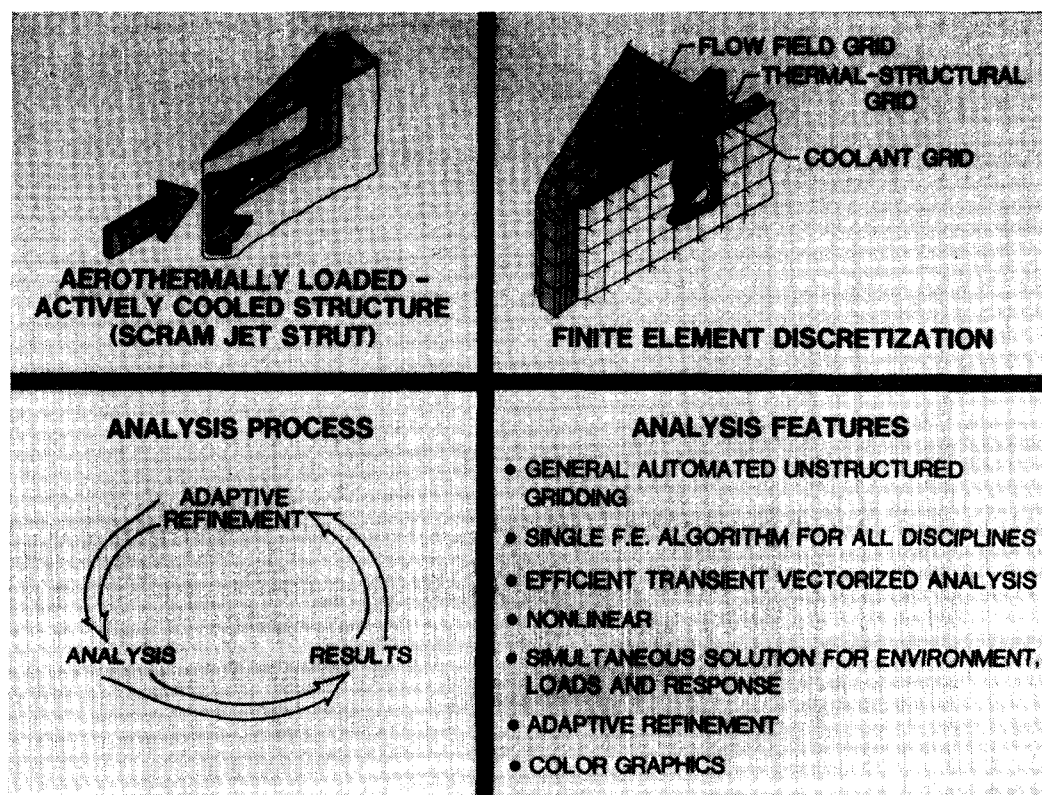


Figure 2

973

# FLUID-THERMAL-STRUCTURAL FORMULATION

The aerodynamic flow equations are described by the conservation of mass, momentum, and energy equations. These equations can be written in conservation form as shown on the left of figure 3. The fluid unknowns are the density $\rho$, the velocity components u and v, and the total energy $\varepsilon$. The flux components, E and F, contain aerothermal terms such as the aerodynamic pressure, wall shear stress , and heat flux, which are of interest to the thermal structural designer.

The thermal and structural equations are also written in conservation form as shown on the right of figure 3. The first two terms in the brackets represent components of the structural equilibrium equations and the last term represents components of the energy equation for the heat transfer in the structure. Nonlinearities due to the temperature dependent material properties and large strain-displacement relations are included. Details of these fluid, thermal, structural equations are given in Ref. 2.
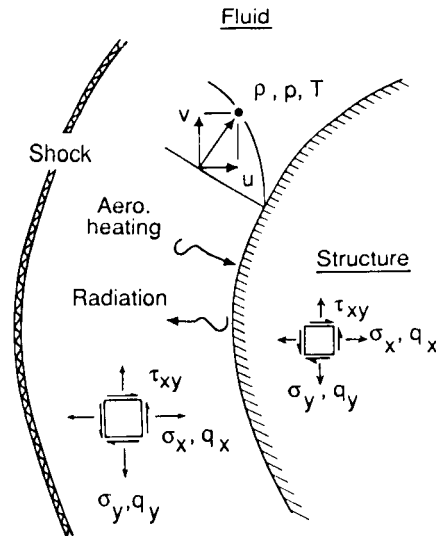
## FLUID ANALYSIS

$$\frac{\partial \{U\}}{\partial t} + \frac{\partial \{E\}}{\partial x} + \frac{\partial \{F\}}{\partial y} = 0$$

$$\{U\} = \begin{Bmatrix} \rho \\ \rho u \\ \rho v \\ \rho \varepsilon \end{Bmatrix}$$

$$\{E\} = \begin{Bmatrix} \rho u \\ \rho u^2 + p \\ \rho u v \\ \rho u \varepsilon + p u \end{Bmatrix}$$

$$+ \begin{Bmatrix} 0 \\ \sigma_x \\ \tau_{xy} \\ u\sigma_x + v\tau_{xy} - q_x \end{Bmatrix}$$

## THERMAL-STRUCTURAL ANALYSIS

$$\frac{\partial \{U\}}{\partial t} + \frac{\partial \{E\}}{\partial x} + \frac{\partial \{F\}}{\partial y} = 0$$

$$\{U\} = \begin{Bmatrix} cu \\ cv \\ \rho c_v T \end{Bmatrix} \quad ; \{E\} = \begin{Bmatrix} -\sigma_x \\ -\tau_{xy} \\ q_x \end{Bmatrix}$$

- c is fictitious damping constant

- Temperature dependent material properties

- Large strain-displacement,

$$\varepsilon_x = \frac{\partial u}{\partial x} + \frac{1}{2}\left(\frac{\partial u}{\partial x}\right)^2 + \frac{1}{2}\left(\frac{\partial v}{\partial x}\right)^2$$

Figure 3

# COWL AEROTHERMAL LOADS AMPLIFIED BY SHOCK-ON-LIP

Leading edges for hypersonic vehicles that experience intense stagnation point pressures and heating rates are a significant challenge to the designer. For engine leading edges, such as the cowl shown in figure 4, intense aerothermal loads occur when the cowl bow shock is intersected by an oblique shock resulting in a supersonic jet that impinges on the leading edge surface. The experimental configuration (lower left of figure), which simulates the vehicle forebody and cowl leading edge, was used to define the aerothermal loads (see Ref. 3). The schlieren photograph shows the supersonic jet interference pattern impinging on the surface of the cylinder. The interference pattern produces intense local amplification of the pressure and heat transfer rate in the vicinity of the jet impingement. The undisturbed (absence of incident oblique shock and interference pattern) stagnation pressure and heat transfer rate can be amplified by factors from 6 to 30 depending on the shock strength and the free stream Mach number (Ref. 3).

The intensity and localization of this phenomena offers a significant challenge to computational fluid dynamics codes which must accurately capture the shock interference pattern and the attendant flow gradients to accurately predict the loads. Therefore this problem and experimental results will be used to demonstrate the integrated fluid-thermal-structural analysis method.
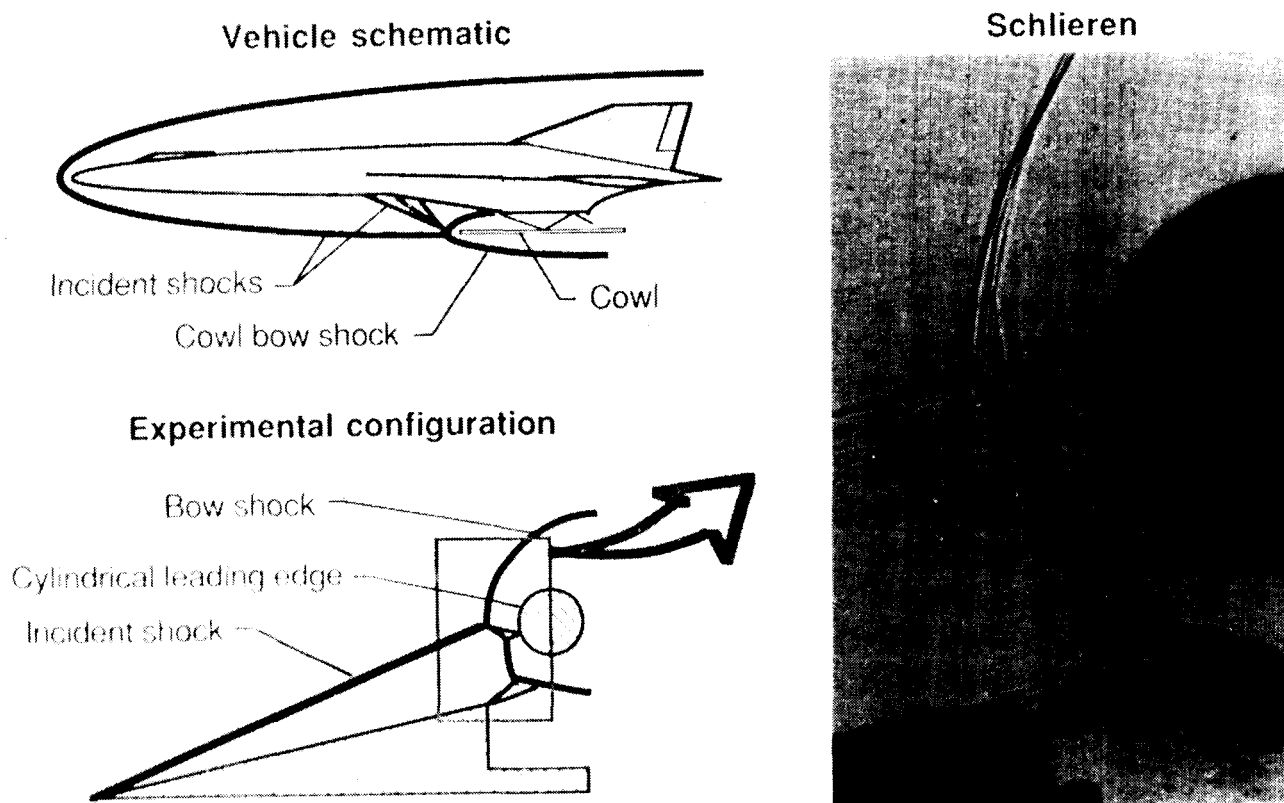


Figure 4

# OBLIQUE AND BOW SHOCK INTERACTION ON CYLINDER

The supersonic jet interference pattern occurs when an oblique shock wave intersects the nearly normal part of the bow shock from the blunt cowl leading edge as shown schematically in figure 5. The intersection results in further displacement of the bow shock and the formation of a supersonic jet contained between two shear layers and submerged within the subsonic shock layer between the body and the bow shock wave. A jet bow shock is produced when the jet impinges on the surface, creating a small region of stagnation heating.

The computational technique and coupling between the fluid and the structure were evaluated using experimental results (Ref. 3) from the oblique and bow shock interaction on a three inch diameter stainless steel cylinder. The computational domain for the flow field and cylinder are shown in figure 5. The inflow conditions above and below the oblique shock are (1) Mach 8.03 flow at an angle of attack of zero degrees ($\theta = 0°$) and a static temperature of 200 °R, and (2) Mach 5.25 flow at an angle of attack of 12.5 degrees ($\theta = -12.5°$) and a static temperature of 430 °R. The supersonic jet impinges on the cylinder surface approximately 20 degrees below the cylinder horizontal centerline.
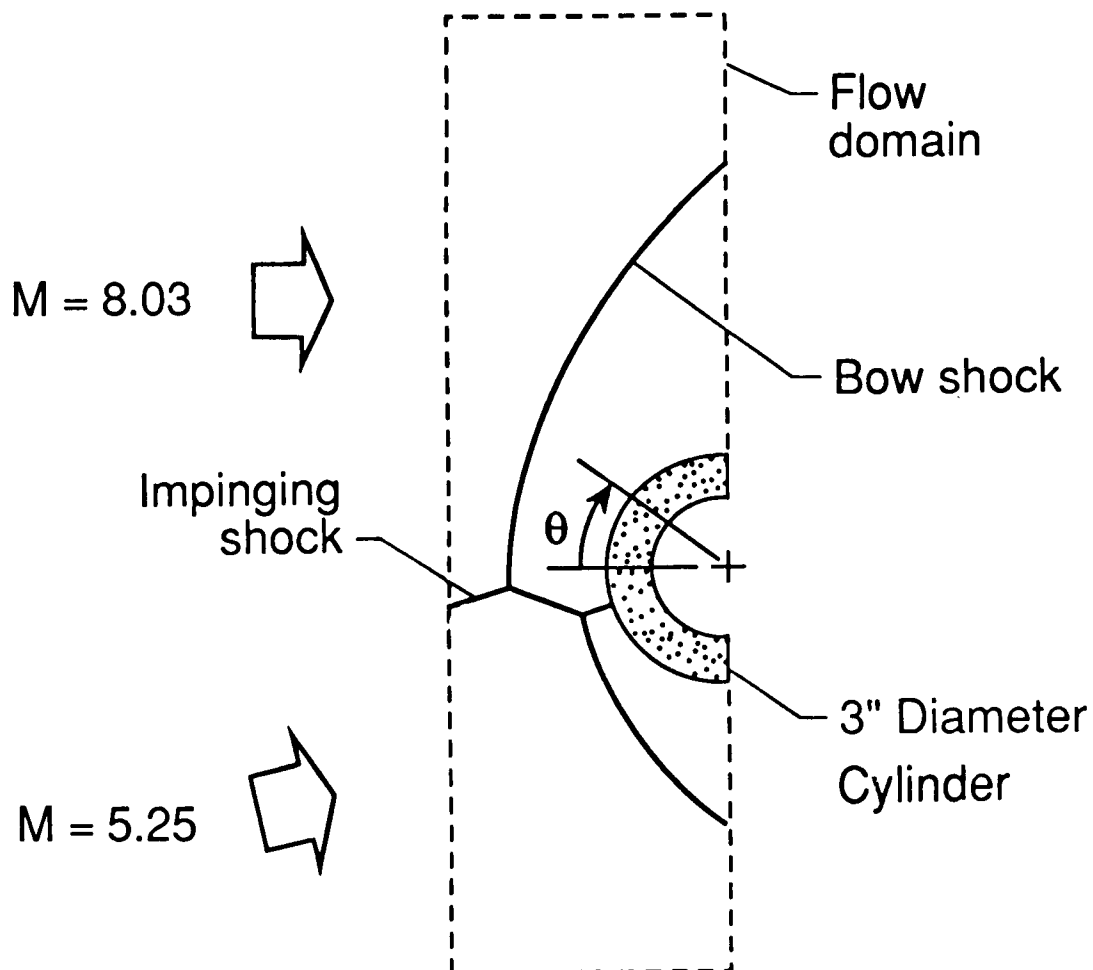


Figure 5

# ADAPTIVE UNSTRUCTURED FINITE ELEMENT MESHES

The adaptive unstructured finite element remeshing technique described in Ref. 4 is used for the discretization of the flow domain to minimize the flow unknowns. Mesh adaptivity based on error indicators obviates a priori knowledge of the flow physics, which is nonexistent for this complex flow phenomena. Unstructured meshes permit adaptivity with fewer grid points than structured adaptivity. For the problem at hand, the three finite element meshes shown in figure 6 were required to obtain an accurate solution. The solution procedure starts from the uniform mesh (first mesh) which consists of triangles in the inviscid flow field and quadrilateral elements in the boundary layer region to obtaining accurate aerodynamic heating rates. As the fluid analysis proceeds, the mesh is adapted to the physics of the flow field. Elements are concentrated in the regions with large gradients (density in this case) and are removed from the regions where the gradients are small. In fact, the mesh density simulates the flow density gradients given by the schlieren shown in figure 4. The base and altitude of the triangular elements are oriented in the principal gradient directions to improve solution accuracy. The evolution of the meshes shown in the figure demonstrates the adaptive remeshing capability which provides the best flow solution with the least number of unknowns. This adaptive unstructured remeshing technique would provide similar benefits for the thermal and structural analyses and are being evaluated.



**3823 nodes**
**5760 elements**

**5926 nodes**
**8083 elements**

**8896 nodes**
**11578 elements**

**First mesh**          **Second mesh**          **Third mesh**
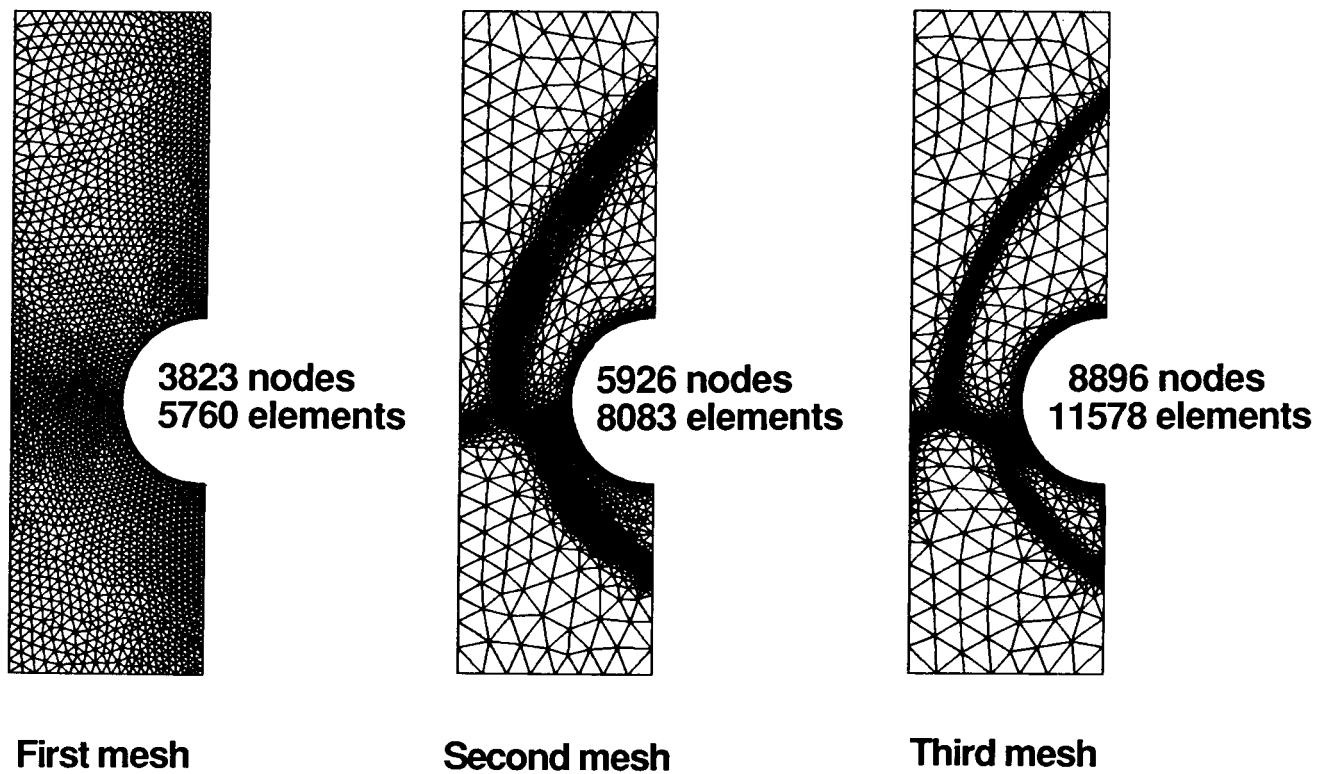
Figure 6

## FLOW MACH NUMBER CONTOURS

The fluid analysis was performed using a point implicit upwinding technique described in Refs. 5 and 6. Using the crude uniform mesh (first mesh) shown in figure 6, the essential features of the flow were captured as indicated by the Mach number contours shown in figure 7. The Mach number contour scale is shown on the right of the figure. Using the density gradients from this first solution as an error indicator, the second mesh shown in figure 6 was created. The same procedure is repeated on subsequent meshes until the converged flow solution is achieved (a total of three meshes in this case).

The Mach number contours shown below demonstrate the improvement in the solution quality as the mesh is adapted. The Mach number distribution obtained on the third mesh clearly shows improved sharpness of the shock interference pattern. As described earlier the supersonic jet is submerged with subsonic regions between the bow shock and the cylinder. The Mach number in the supersonic jet is approximately two. The supersonic flow in the jet terminates through a nearly normal shock prior to impinging on the cylinder surface. The accuracy of the aerothermal loads on the cylinder surface are highly dependent on the fidelity of the shock interference pattern which is primarily an inviscid flow feature.

|   |           |
|---|-----------|
|   | 0.386E−12 |
| A | 0.402E+00 |
|   | 0.803E+00 |
|   | 0.120E+01 |
|   | 0.161E+01 |
| B | 0.201E+01 |
|   | 0.241E+01 |
|   | 0.281E+01 |
|   | 0.321E+01 |
| C | 0.361E+01 |
|   | 0.402E+01 |
|   | 0.442E+01 |
|   | 0.482E+01 |
| D | 0.522E+01 |
|   | 0.562E+01 |
|   | 0.602E+01 |
|   | 0.642E+01 |
| E | 0.683E+01 |
|   | 0.723E+01 |
|   | 0.763E+01 |

**First mesh**          **Second mesh**          **Third mesh**

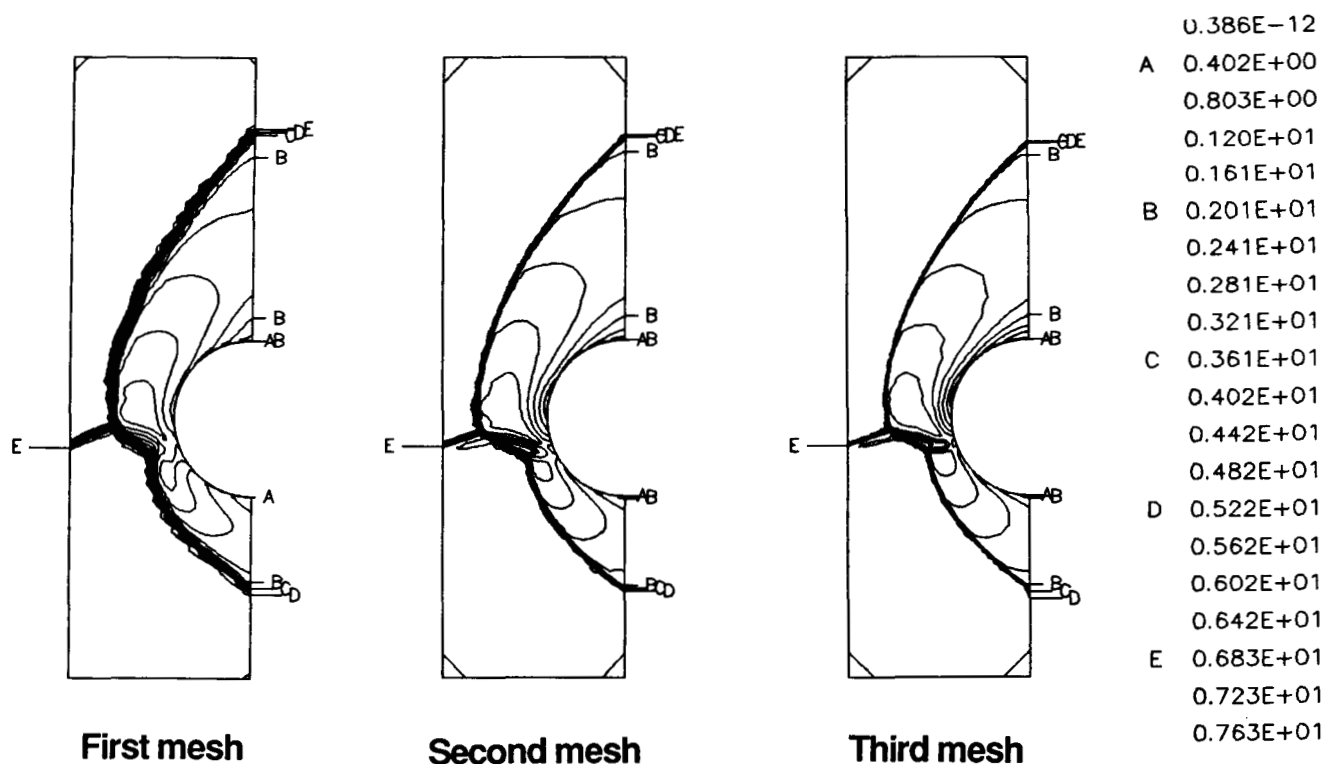Figure 7

# FLOW PRESSURE CONTOURS

The flow field pressure contours from the three meshes are shown in figure 8. The pressure contour scale in psia is shown on the right of the figure. The free stream flow pressure is 0.143 psia. The pressure increases to approximately 10 psia across the bow shock but jumps abruptly to 75 psia across the jet normal shock where the supersonic jet impinges on the cylinder. The surface pressure distribution is shown in figure 9.
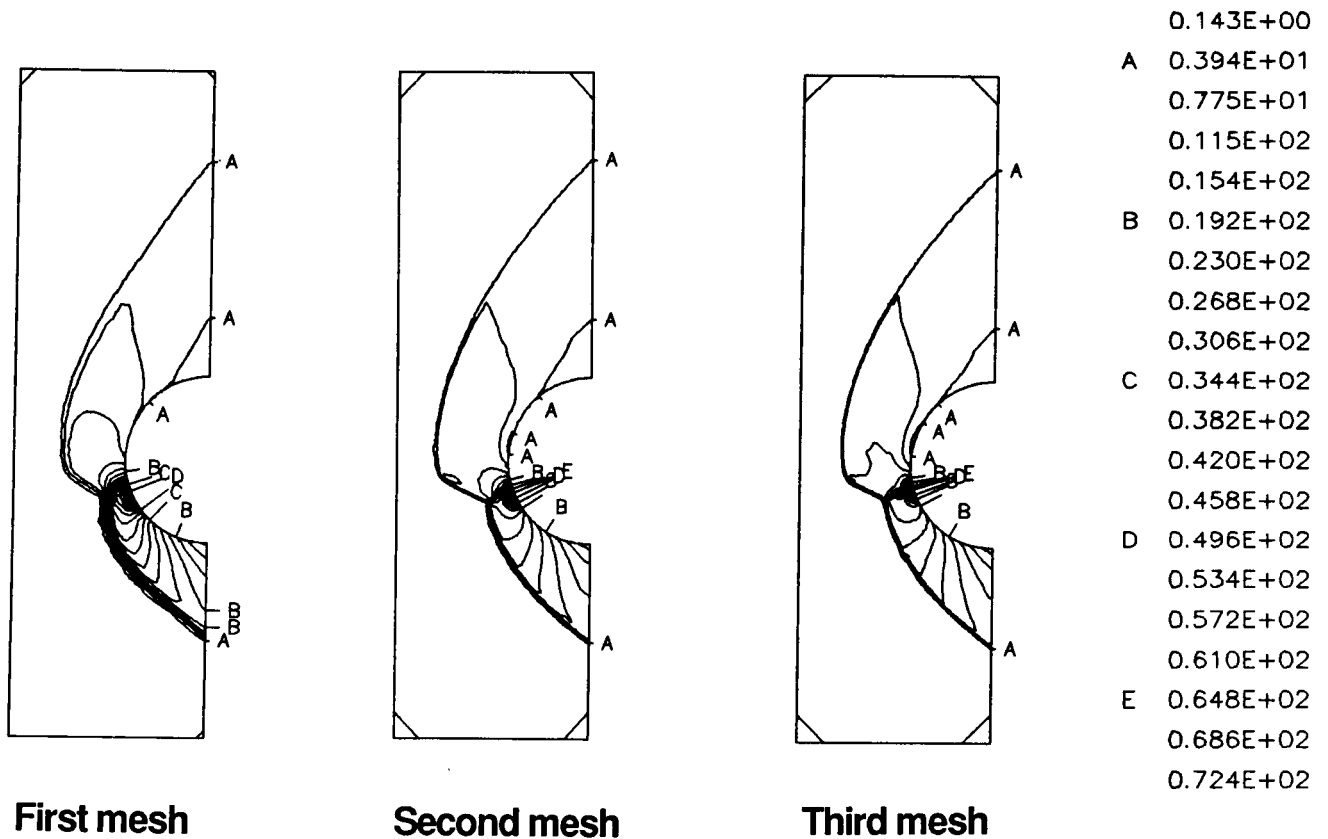
| | |
|---|---|
| | 0.143E+00 |
| A | 0.394E+01 |
| | 0.775E+01 |
| | 0.115E+02 |
| | 0.154E+02 |
| B | 0.192E+02 |
| | 0.230E+02 |
| | 0.268E+02 |
| | 0.306E+02 |
| C | 0.344E+02 |
| | 0.382E+02 |
| | 0.420E+02 |
| | 0.458E+02 |
| D | 0.496E+02 |
| | 0.534E+02 |
| | 0.572E+02 |
| | 0.610E+02 |
| E | 0.648E+02 |
| | 0.686E+02 |
| | 0.724E+02 |

**First mesh**        **Second mesh**        **Third mesh**

Figure 8

# SURFACE PRESSURE DISTRIBUTION

The analytically predicted surface pressure distribution from the third mesh is compared with the experimentally measured pressures in figure 9. The predicted and experimental pressures are normalized by the undisturbed stagnation pressure ($p_0$ = 10.61 psia). The figure shows good agreement of the pressure distributions, peak pressure ( 82 ± 5 psia versus a predicted value of 75 psia) and excellent agreement of the peak pressure locations ( $\theta$ = - 19.1° vs. a prediction of - 20°). The predicted pressure distribution is applied as a static load on the cylinder for the structural analysis to be presented later.
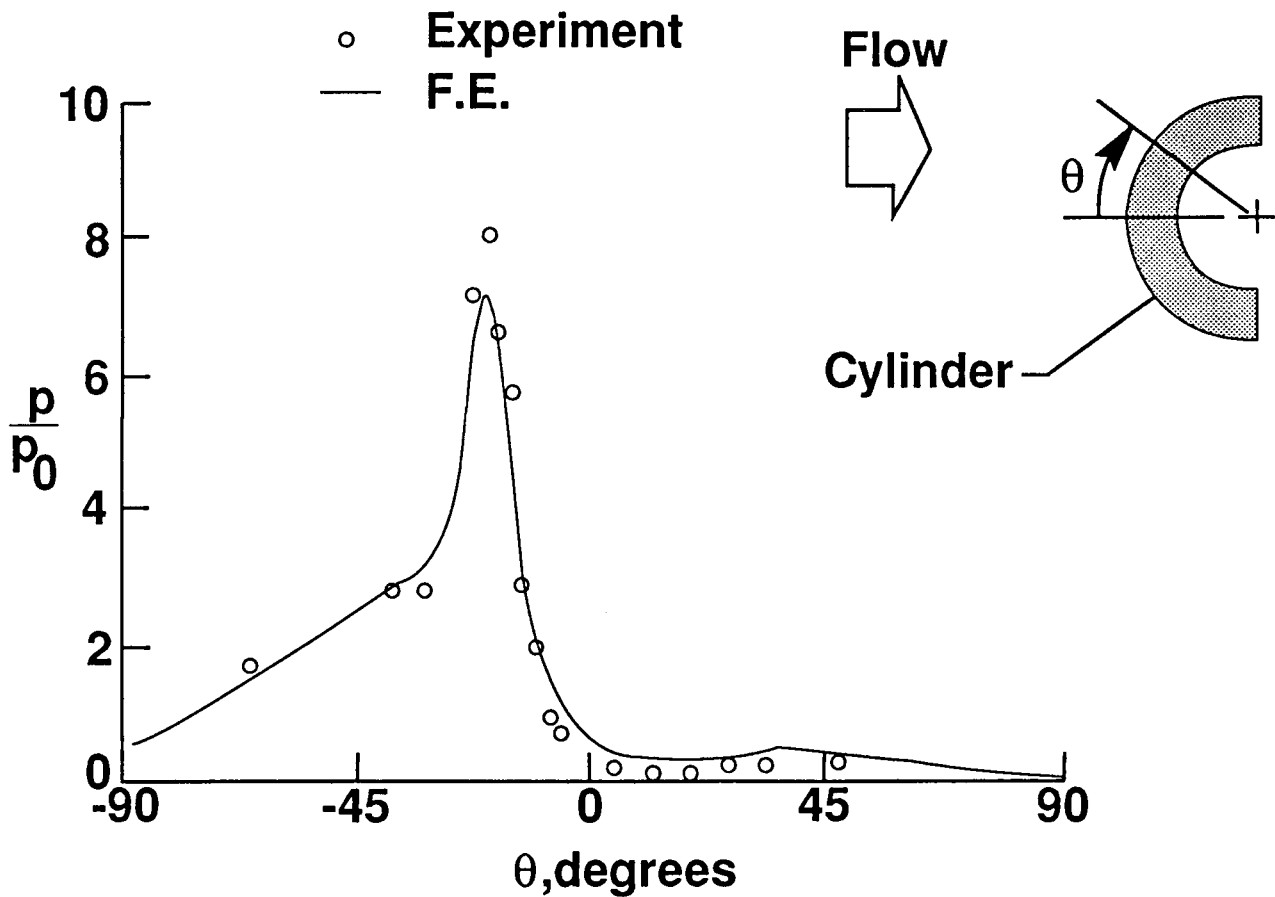


Figure 9

## FLOW TEMPERATURE CONTOURS

The flow static temperature contours for the three meshes are shown in figure 10. The temperature contour scale in °R is shown on the right of the figure. The flow temperature increases abruptly from approximately 200 °R to a maximum of 3000 °R across the normal part of the bow shock, remains almost uniform, and drops sharply through the boundary layer to the cylinder surface temperature resulting in high aerodynamic heating rates. A more detailed view of the temperature contours in the interaction region is presented in figure 11.
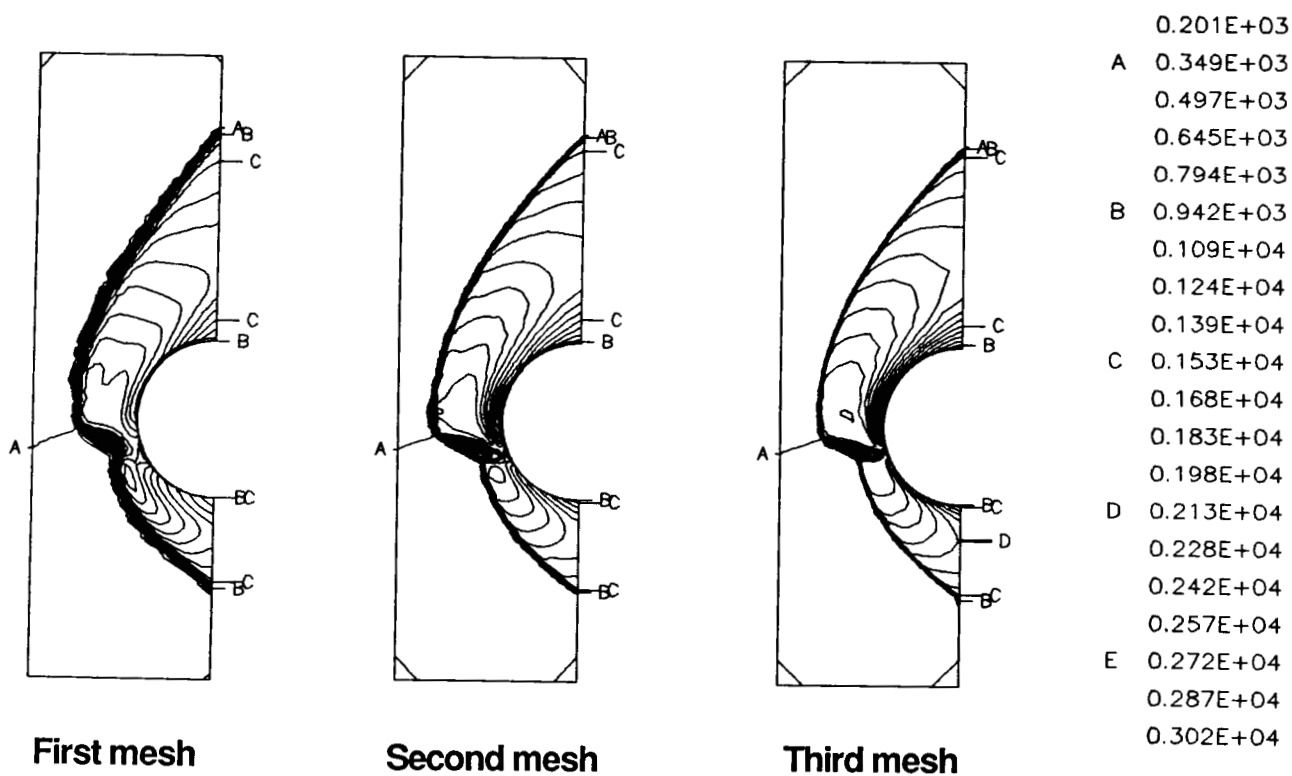


| | |
|---|---|
| | 0.201E+03 |
| A | 0.349E+03 |
| | 0.497E+03 |
| | 0.645E+03 |
| | 0.794E+03 |
| B | 0.942E+03 |
| | 0.109E+04 |
| | 0.124E+04 |
| | 0.139E+04 |
| C | 0.153E+04 |
| | 0.168E+04 |
| | 0.183E+04 |
| | 0.198E+04 |
| D | 0.213E+04 |
| | 0.228E+04 |
| | 0.242E+04 |
| | 0.257E+04 |
| E | 0.272E+04 |
| | 0.287E+04 |
| | 0.302E+04 |

**First mesh**        **Second mesh**        **Third mesh**

Figure 10

# FLOW TEMPERATURE CONTOURS IN INTERACTION REGION

Details of the finite element mesh and the flow temperature in the interaction region are shown in figure 11. On both sides of the supersonic jet, the fluid temperature increases abruptly across the bow shocks from a relatively low temperature (200 °R and 430 °R) to approximately 2,700 °R. The temperature gradients in the shock layer (region between the bow shock and the cylinder) are relatively small except in the thin boundary layer where the temperature drops sharply to the cylinder surface temperature of 530 °R . Inside the supersonic jet, the fluid temperature increases slightly from the free stream temperature to approximately 1200 °R. As the jet stream approaches the cylinder surface, the fluid temperature increases abruptly across the jet normal shock to approximately 3,000 °R in a small stagnation region next to the cylinder surface and drops sharply to the cylinder temperature of 530°R. The high temperature gradients in this region result in a high localized aerodynamic heating rate at the jet impingement location. The severity of the temperature gradients is depicted in figure 12.
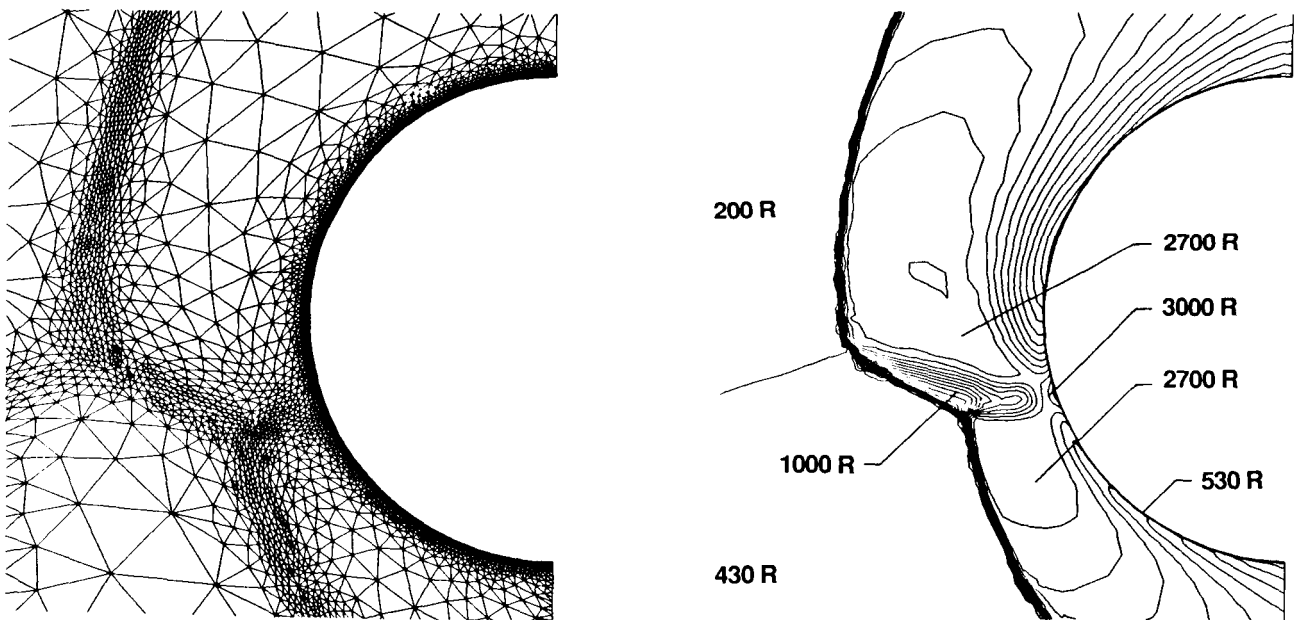
Figure 11

982

# FLOW TEMPERATURE DISTRIBUTION

The fluid temperature distribution along a line below the supersonic jet is shown in figure 12 to highlight the severity of the temperature gradients across the shock and the thin boundary layer next to the cylinder surface. The gradient across the shock wave and boundary layer are approximately the same. These large temperature gradients require closely spaced elements for accuracy particularly in the boundary layer to accurately capture the aerodynamic heating rates. These fine meshes place severe constraints on the computational procedure since small time steps are normally required to assure solution stability. Therefore adaptive unstructured meshes, which significantly reduce the number of solution unknowns, improve solution tractability.
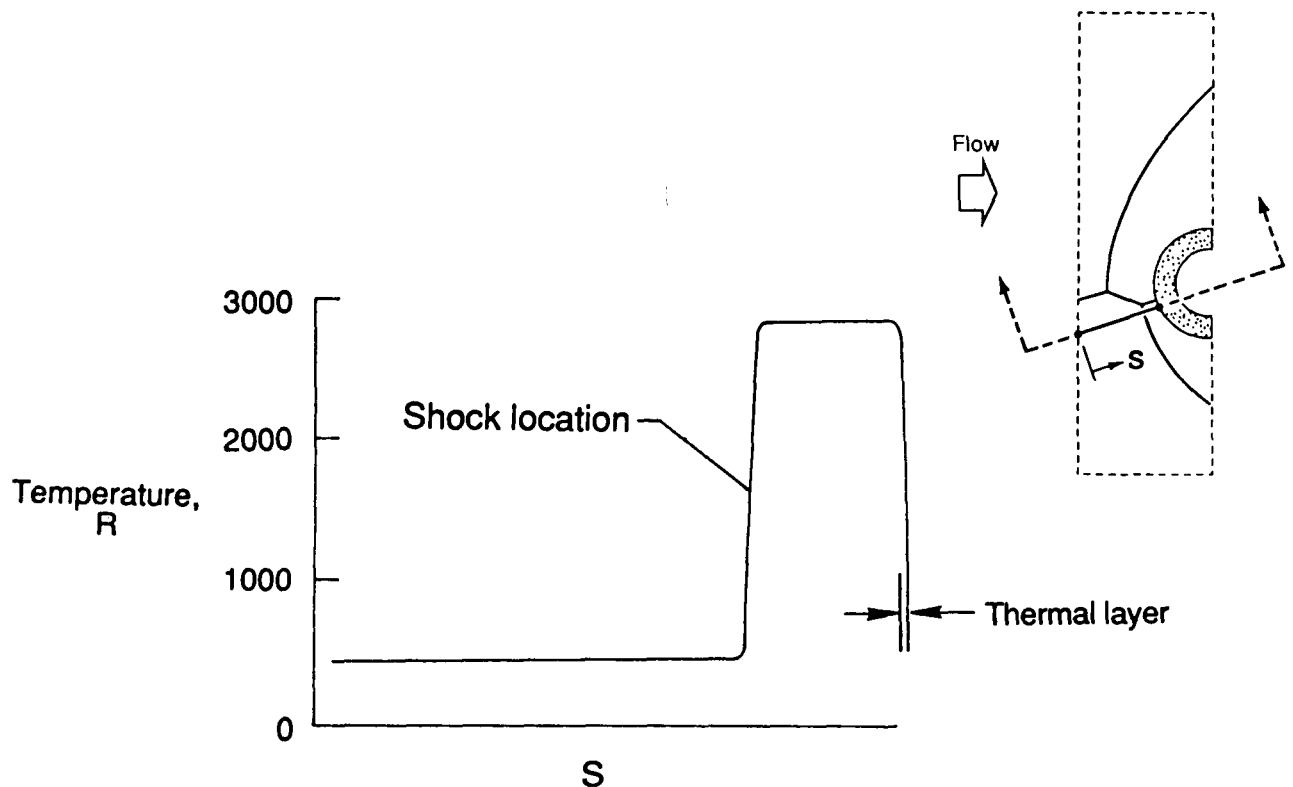


Figure 12

# SURFACE HEATING RATES

The analytical and experimental heating rate distributions normalized to their respective undisturbed stagnation point heating rate are compared in figure 13. The predicted stagnation heating rate of 41.4 Btu/ft$^2$-sec, which was obtained from a viscous shock layer solution, is lower than the experimental value of 61.7 Btu/ft$^2$-sec (see Ref. 2). The difference between the predicted and experimental stagnation point heating rates is attributed to free stream turbulence emanating into the test stream from the turbulent boundary layer on the nozzle. Since this free stream turbulence is present during both the undisturbed (no impinging shock) and during the shock interaction test, normalization would tend to attenuate the effect of the free stream turbulence, hence providing a better comparison with the analytical predictions which do not account for any turbulence.

The heating rate distributions are in reasonably good agreement; however, the peak amplification is underpredicted as well as the heating rates between $\theta = -30°$ and $-55°$. The underprediction is attributed to turbulence in the shear layers that bound the supersonic jet and transition of the boundary layer from laminar to turbulent. Neither of these two effects are accounted for in the analysis which is laminar. These aerodynamic heating rates are applied to the structure in the thermal analysis to predict the cylinder temperature distribution. The temperature distribution is then used in the thermal stress analysis and as a boundary condition for an updated flow analysis to account for the effect of the surface temperature on the aerodynamic heating rates.
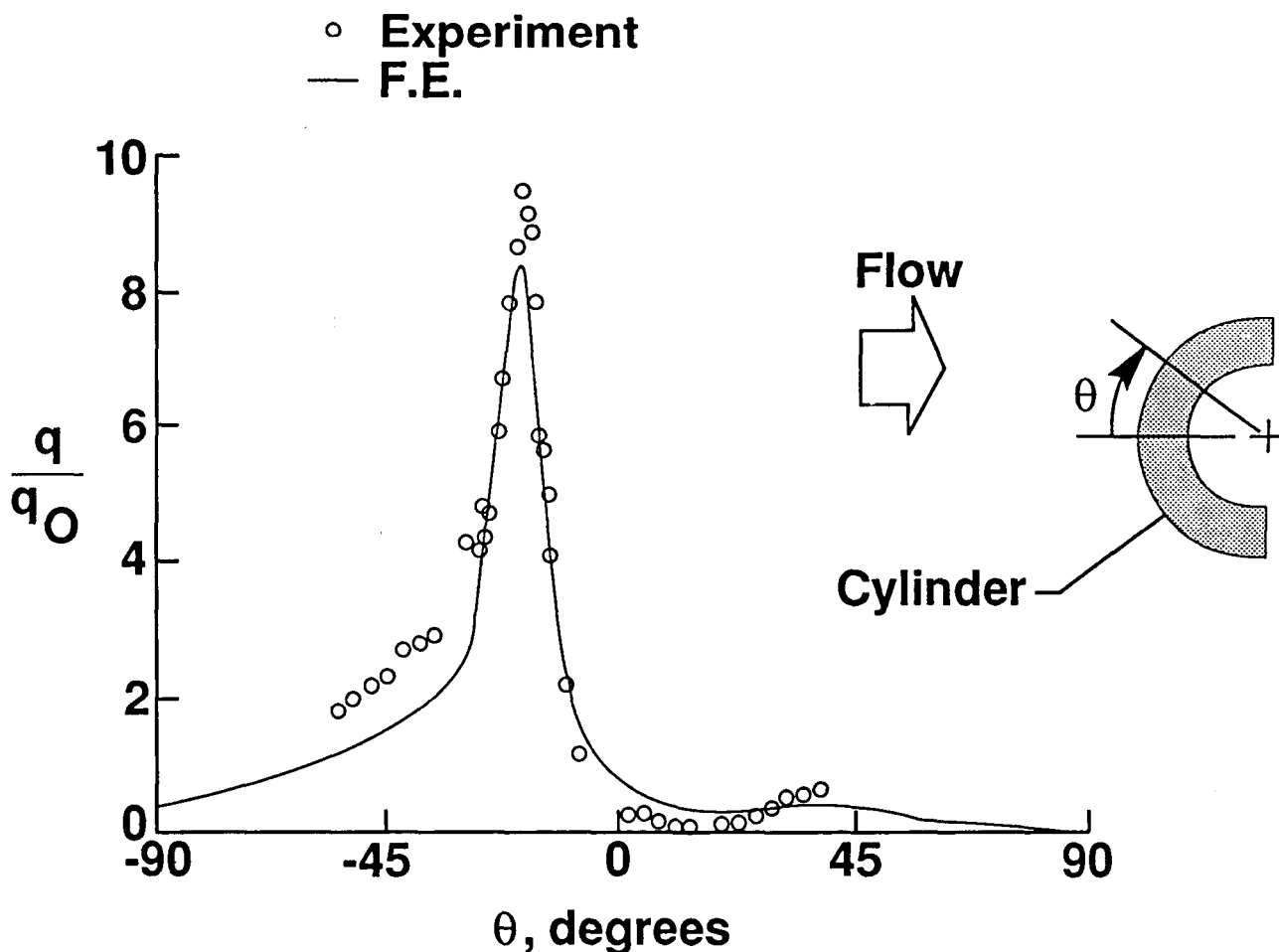


Figure 13

# CYLINDER FINITE ELEMENT MODEL

The cylinder geometry, boundary conditions, and the finite element thermal-structural model are shown in figure 14. The cylinder is made of AM-350 stainless steel in which the material properties such as the thermal conductivity, specific heat, Young's modulus, thermal expansion coefficient, etc. are temperature dependent. The cylinder outer surface is subjected to aerodynamic pressure (figure 9) and heating rate (figure 13) obtained from the fluid analysis. The surface emits radiant energy to the surrounding medium at a temperature of 430 °R. The same finite element discretization is used for both thermal and structural analyses so that the difficulty in transferring data is eliminated. The mesh is graded radially from a very fine spacing at the surface to a coarser spacing on the inner surface. A common discretization is used circumferentially along the fluid and the cylinder interface to eliminate the data manipulation often required between different disciplinary analyses. Both thermal and structural analyses of the cylinder were performed using a one-step Taylor-Galerkin finite element analysis technique ( Ref. 2).
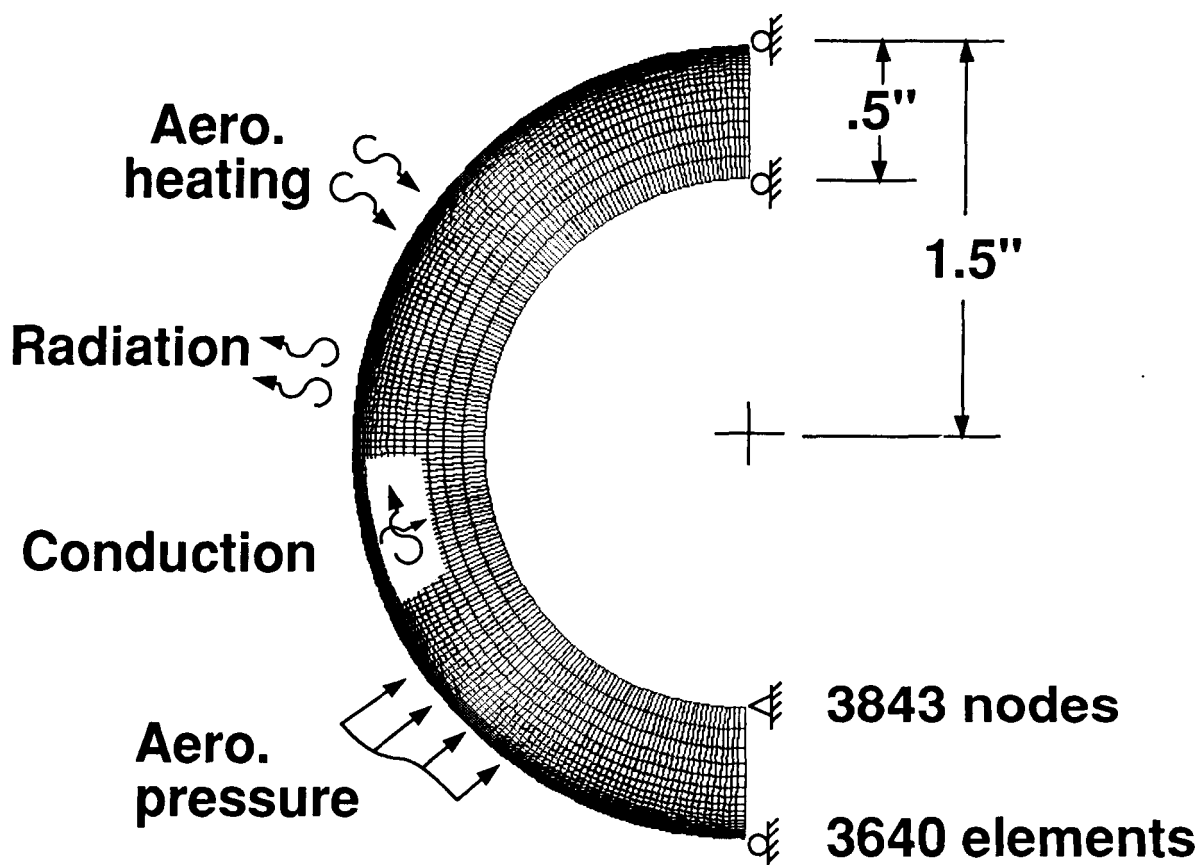


Figure 14

## CYLINDER TEMPERATURE AT 0.5 SECOND

The cylinder temperature contours at 0.5 second are shown in the figure 15. The temperature contour scale in °R is shown on the right of the figure. The maximum temperature is about 1,100°R and occurs at the supersonic jet impingement location. The temperature away from this small impingement region remains at the ambient temperature of 530 °R. The intense local aerodynamic heating rates generated by the supersonic jet stream result in these high temperatures and temperature gradients in the jet impingement region after only a short exposure. The high temperature and temperature gradients result in the high thermal stresses shown in figure 16.

The response of a flight weight leading edge for the National Aero-Space Plane, which is exposed to extremely high aerodynamic heating rates during shock-on-lip conditions, is very rapid. In fact the response time is approaching the response time of the flow field and therefore may require a coupled fluid thermal analysis.

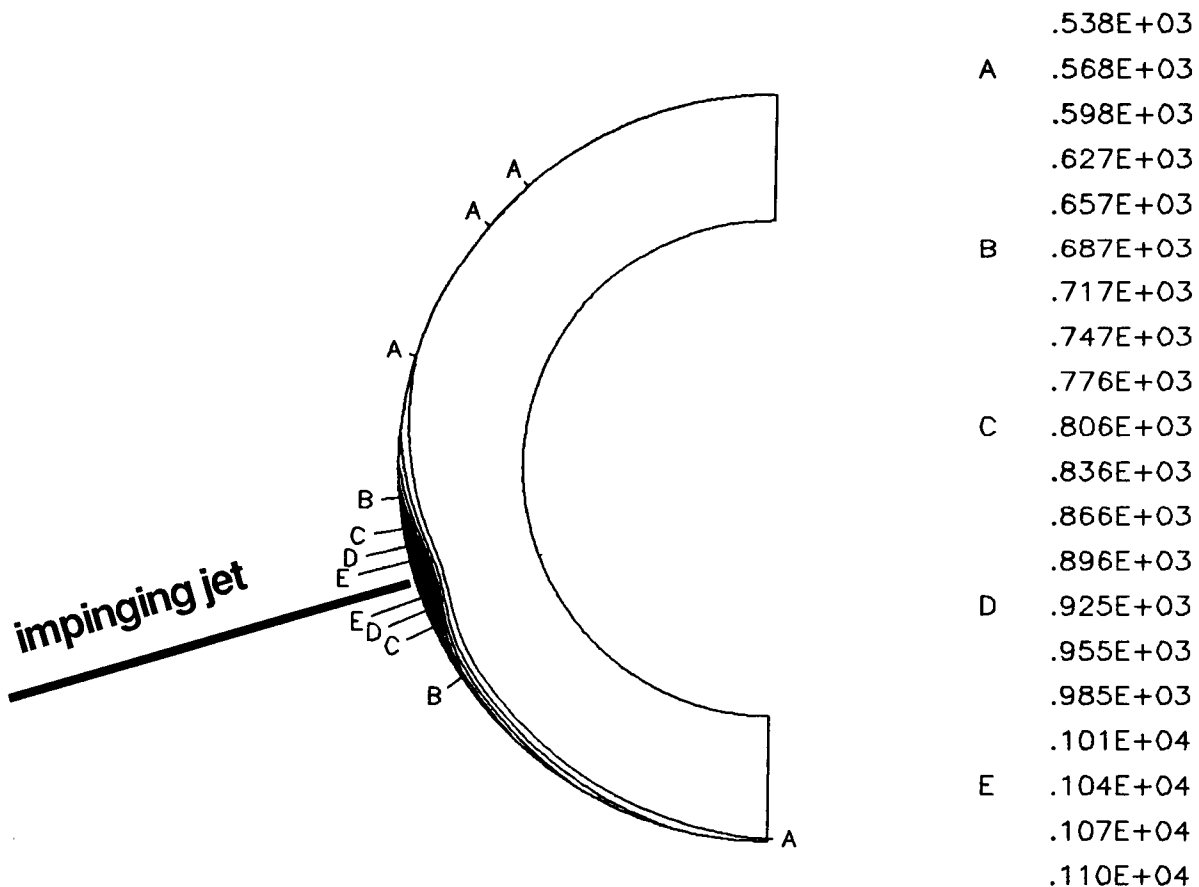|   |          |
|---|----------|
|   | .538E+03 |
| A | .568E+03 |
|   | .598E+03 |
|   | .627E+03 |
|   | .657E+03 |
| B | .687E+03 |
|   | .717E+03 |
|   | .747E+03 |
|   | .776E+03 |
| C | .806E+03 |
|   | .836E+03 |
|   | .866E+03 |
|   | .896E+03 |
| D | .925E+03 |
|   | .955E+03 |
|   | .985E+03 |
|   | .101E+04 |
| E | .104E+04 |
|   | .107E+04 |
|   | .110E+04 |

Figure 15

impinging jet

C - 6

# CIRCUMFERENTIAL STRESS ON DEFORMED CYLINDER AT 0.5 SECOND

The circumferential stress distribution superimposed on the deformed cylinder at 0.5 second is shown in figure 16. The stress contour scale in psia is shown on the right of the figure. The structural analysis was performed assuming quasi-static and plane strain behavior. The structural loads include the temperature distribution shown in figure 15 and the aerodynamic pressure shown in figure 9. The maximum deformation of 0.001 inch is radial and occurs at the jet impingement location. This maximum deformation is small and is assumed to have negligible effect on the flow field. The cylinder deformations are greatly exaggerated to highlight the deformed shape. The peak compressive circumferential stress of approximately 60 ksi occurs at the jet impingement location where the temperature and temperature gradients are maximum. The axial stresses, which are much larger than the circumferential stress, exceed the elastic limit. Hence, longer exposure with attendant higher temperature and stresses could result in permanent deformations and failure of the cylinder. Therefore a more sophisticated structural analysis, such as the capability to predict the permanent localized deformation including time dependency effects, is needed. Currently, the application of a unified viscoplastic theory for accurate prediction of the structural response at higher temperature is under investigation.
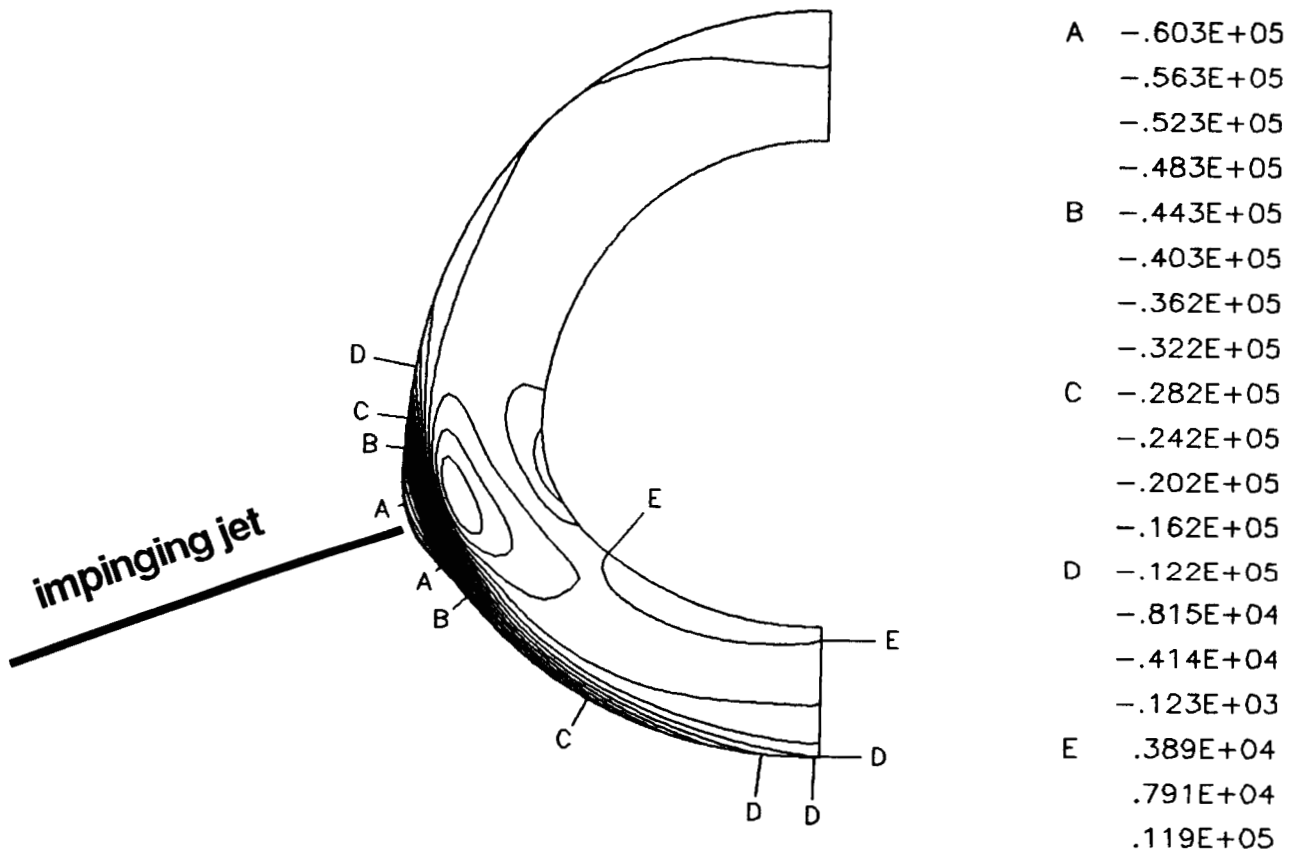


| | |
|---|---|
| A | $-.603E+05$ |
| | $-.563E+05$ |
| | $-.523E+05$ |
| | $-.483E+05$ |
| B | $-.443E+05$ |
| | $-.403E+05$ |
| | $-.362E+05$ |
| | $-.322E+05$ |
| C | $-.282E+05$ |
| | $-.242E+05$ |
| | $-.202E+05$ |
| | $-.162E+05$ |
| D | $-.122E+05$ |
| | $-.815E+04$ |
| | $-.414E+04$ |
| | $-.123E+03$ |
| E | $.389E+04$ |
| | $.791E+04$ |
| | $.119E+05$ |

Figure 16

# SURFACE HEATING RATES AFTER 0.5 SECOND OF EXPOSURE

The aerodynamic heating rates and hence the flow field are coupled to the thermal response of the cylinder through the energy equation. As the cylinder surface temperature increases, the thermal gradient through the boundary layer decreases, resulting in lower heating rates. The cylinder surface temperature after 0.5 second of exposure was used to update the aerodynamic analysis. The peak aerodynamic heating rate decreased nearly 50% from the initial heating rate at 0 second when the cylinder wall was isothermal at 530°R. The time interval of 0.5 second was selected to highlight the coupling effect between the aerodynamic flow and the cylinder thermal-structural response. A more accurate coupled fluid-thermal-structural solution can be obtained by decreasing the time interval and updating the different disciplinary analyses more frequently. Simultaneous solution of the flow field and the thermal response of the cylinder would be ideal; however, the extremely fine grid required for the flow analysis results in small time steps to insure solution stability. A time accurate transient solution would require the use of these small time steps throughout the flow solution domain and would be prohibitively expensive. The present solution avoids this dilemma by using local time stepping ( time step for each element set by stability requirements) and marching the solution to steady state. This process is valid as long as the structure thermal response is much slower than the flow field response, which is usually the case.
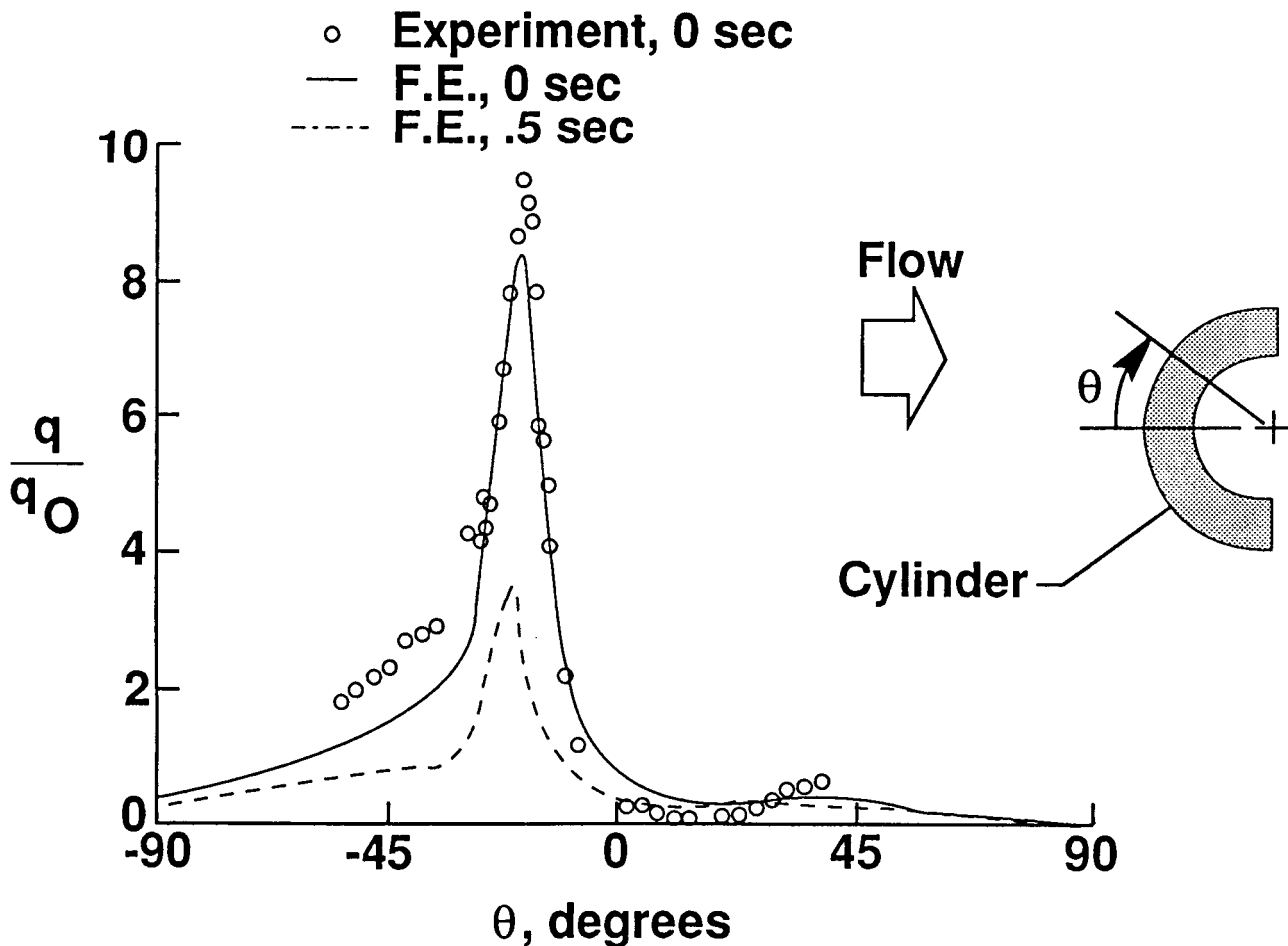


Figure 17

## CONCLUDING REMARKS

An integrated fluid-thermal-structural finite element analysis approach was demonstrated for a cylinder subjected to shock wave interference heating. A general automated unstructured gridding was used to discretize the aerodynamic flow field to minimize the number of unknowns and provide an accurate and economical analytical solution. The finite element method is used in the three disciplinary analyses to facilitate the interdisciplinary data exchange. Coupling between the aerodynamic flow, the thermal, and structural response is included in the procedure; however, for Mach 8 shock wave interference on a three inch diameter stainless steel cylinder the coupling is limited to the effect of the surface temperature on the aerodynamic heating rates. The prediction of the flow behavior and the aerodynamic pressures and heating rates are in good agreement with experiment. The application has demonstrated the capability of this integrated fluid-thermal-structural analysis approach to (1) provide solutions to complex aerothermostructural behavior, (2) reduce manpower requirements, and (3) increase the computational efficiency for coupled interdisciplinary problems.

- INTEGRATED FLUID-THERMAL-STRUCTURAL FINITE ELEMENT ANALYSIS CAPABILITY DESCRIBED.

- AUTOMATED ADAPTIVE UNSTRUCTURED GRIDDING USED FOR MINIMUM PROBLEM SIZE.

- FINITE ELEMENT ALGORITHM PROVIDES SOLUTION FOR ALL THREE DISCIPLINES.

- COUPLING BETWEEN F-T-S INCLUDED FOR MULTIDISCIPLINARY INTERACTION.

- INTEGRATED F-T-S APPROACH REDUCES MANPOWER AND INCREASES COMPUTATIONAL EFFICIENCY.

Figure 18

# REFERENCES

1.  Wieting, A. R.; Dechaumphai, P.; Bey, K. S. ; Thornton, E. A. and Morgan, K.: "Application of Integrated Fluid-Thermal-Structural Analysis Methods," Presented at the 16th Congress of the International Council of the Aeronautical Sciences, Jerusalem, Israel, August 28 - September 2, 1988.

2.  Dechaumphai, P.; Thornton, E. A. and Wieting, A. R.: "Flow-Thermal-Structural Study of Aerodynamically Heated Leading Edges," Presented at the AIAA/ASME/ASCE/AHS 29th Structures, Structural Dynamics and Materials Conference, Williamsburg, Virginia, April 18-20, 1988, AIAA Paper No. 88-2245-CP.

3.  Wieting, A. R. and Holden, M. S.: "Experimental Study of Shock Wave Interference Heating on a Cylinder Leading Edge," Presented at the AIAA 22nd Thermophysics Conference, Honolulu, Hawaii, June 8-10, 1988, AIAA Paper No. 87-1511.

4.  Peraire, J; Vahdati, M.; Morgan, K. and Zienkiewicz, O. C.: "Adaptive Remeshing for Compressible Flow Computations," Journal of Computational Physics, Volume 72, pp. 449-466, 1987.

5.  Thareja, R. R.; Stewart, J. R.; Hassan, O.; Morgan, K. and Peraire, J.: "A Point Implicit Unstructured Grid Solver for the Euler and Navier-Stokes Equations," Presented at the AIAA 26th Aerospace Sciences Meeting, Reno, Nevada, January 11-14, 1988, AIAA Paper No. 88-0036.

6.  Gnoffo, P. A.: "Application of Program LAURA to Three-Dimensional AOTV Flowfields," Presented at the AIAA 24th Aerospace Meeting, Reno, Navada, January 6-9, 1986, AIAA Paper No. 86-0565.